

Direct optimization of neoclassical ion transport in stellarator reactors

B. F. Lee¹, S. A. Lazerson², H. M. Smith³, C. D. Beidler³, and N. A. Pablan⁴

¹ Princeton University, Princeton, New Jersey, U.S.A.

² Gauss Fusion GmbH, Hanau, Germany

³ Max Planck Institute for Plasma Physics, Greifswald, Germany

⁴ Princeton Plasma Physics Laboratory, Princeton, New Jersey, U.S.A.

E-mail: bflee@princeton.edu, samuel.lazerson@gauss-fusion.com, hakan.smith@ipp.mpg.de, craig.beidler@ipp.mpg.de, npablan@pppl.gov

June 2024

Abstract. We directly optimize stellarator neoclassical ion transport while holding neoclassical electron transport at a moderate level, creating a scenario favorable for impurity expulsion and retaining good ion confinement. Traditional neoclassical stellarator optimization has focused on minimizing ϵ_{eff} , the geometric factor that characterizes the amount of radial transport due to particles in the $1/\nu$ regime. Under expected reactor-relevant conditions, core electrons will be in the $1/\nu$ regime and core fuel ions will be in the $\sqrt{\nu}$ regime. Traditional optimizations thus minimize electron transport and rely on the radial electric field (E_r) that develops to confine the ions. This often results in an inward-pointing E_r that drives high- Z impurities into the core, which may be troublesome in future reactors. In our optimizations, we increase the ratio of the thermal transport coefficients L_{11}^e/L_{11}^i , which previous work has shown can create an outward-pointing E_r . This effect is very beneficial for impurity expulsion. We obtain self-consistent density, temperature, and E_r profiles at reactor-relevant conditions for optimized equilibria. These equilibria are expected to enjoy significantly improved impurity transport properties. We conclude by providing several directions of future research that may help further improve the presented optimization algorithm.

Keywords: Nuclear Fusion, Stellarator, Optimization, Neoclassical, Impurity Transport, Electron Root, Electric Field

Submitted to: *Nucl. Fusion*

1. Introduction

Stellarator reactors are expected to achieve relatively high temperatures in their plasma cores, resulting in the electrons and fuel ions exhibiting neoclassical transport characteristics of the long mean free path (lmfp) regime. This regime may be divided into several pieces that can be visualized in figure 12 of reference [1]. The $1/\nu$ regime

corresponds to zero normalized $\mathbf{E}_r \times \mathbf{B}$ drift velocity, $v_E^* \equiv |E_r|/vB_0 = 0$, where $\mathbf{E}_r = E_r(r)\nabla r$ is the radial electric field, r is a flux label, v is particle speed, and B_0 is a reference magnetic field strength. The radial particle and heat transport in the $1/\nu$ regime can be characterized by the magnitude of the geometric factor ϵ_{eff} [2], which has been commonly used as a minimization target for neoclassical stellarator optimizations. If $v_E^* > 0$, two other lmfp regimes exist: the ν regime at extremely low collisionalities and the $\sqrt{\nu}$ regime at more moderate collisionalities. The thermal transport coefficients for particle and heat fluxes are approximately proportional to $|E_r|^{-2}$ in the former case and $|E_r|^{-3/2}$ in the latter [3]. Roughly speaking, $\mathbf{E}_r \times \mathbf{B}$ rotation helps limit the radial excursions of particles from flux surfaces when particle behavior is not entirely dominated by collisional effects. Since ϵ_{eff} characterizes transport levels when $v_E^* = 0$, lowering ϵ_{eff} lowers the “ceiling” on radial transport for populations in all lmfp regimes and thus reduces overall radial transport. However, because $v_E^* \approx 0$ only for electrons under expected reactor-relevant conditions, minimizing ϵ_{eff} directly minimizes only radial electron transport. One may think that radial ion transport would be larger than radial electron transport — the larger ion masses lead to larger radial excursion of the orbits and therefore larger diffusion coefficients — but the charge separation immediately establishes the aforementioned \mathbf{E}_r to make the transport ambipolar [4]. The electric field will point radially inward in this case ($E_r < 0$). Because the ambipolar \mathbf{E}_r is determined by the condition that the net radial current is zero and the ions are the primary contributor to the radial current in (reasonably) low- ϵ_{eff} configurations, the $E_r < 0$ solution of the ambipolarity condition is typically referred to as the “ion root” ambipolar electric field.

In design studies, stellarator reactors have commonly targeted ϵ_{eff} values in the range $0.1\% - 1\%$ [5, 6], which is sufficiently small to prevent neoclassical energy losses from being an obstacle to ignition but not small enough to preclude other design objectives from being taken into account. Such reactors are expected to have strong ion root electric fields, so impurities (e.g., partially-ionized tungsten atoms from the divertor and other plasma-facing components) would be driven into the core and cause substantial radiative losses that would likely make continuous reactor operation difficult. The presence of a neoclassical impurity pinch has long been recognized in the literature [7, 8, 9, 10, 11], and several remedies have been proposed. For instance, the temperature gradient of the fuel ions may help counteract the pinch associated with a small ion root electric field [12, 13], but this will likely not be effective if a strong ion root is present throughout the plasma. Furthermore, tangential electric fields may make this effect relatively unhelpful as they often enhance the impurity pinch caused by the radial electric field, especially for high-Z impurities [14, 15, 16, 17]. Buller et al. attempted to directly optimize the tangential electric field (through the electric potential) to prevent inward impurity flux but were only able to reduce it [18].

Another possible solution exists for the impurity transport problem: if $E_r > 0$ in some region of the plasma, this will provide a thermodynamic force that drives impurities (especially those with high Z) radially out of that region. The case $E_r > 0$ is referred

to as the “electron root” solution of the ambipolarity condition. Operating stellarators with an electron root was historically considered superior to ion root operation since the larger $|E_r|$ characteristic of the electron root is favorable for confinement [19, 20]. On the other hand, experimental realizations of the electron root typically involve substantial electron heating that causes the electron temperature to be much higher than the fuel ion temperature [9, 21, 22, 23, 24], which contradicts the desire for reactors to have strong collisional coupling such that plasma thermal energy efficiently drives fusion reactions. This has lead to skepticism that stellarator reactors can feasibly operate with a steady-state electron root.

In this work, we seek to show that the electron root may not be as elusive in reactors as previously thought. Under the assumptions that transport processes are radially local and the drift kinetic equation can be linearized about a Maxwellian, the neoclassical particle flux may be written as

$$\Gamma_s^{\text{neo}} = -n_s L_{11}^s \left(\frac{n'_s}{n_s} - \frac{q_s E_r}{T_s} + \left(\frac{L_{12}^s}{L_{11}^s} - \frac{3}{2} \right) \frac{T'_s}{T_s} \right), \quad (1)$$

where $q_s = Z_s e$ (with e being the elementary charge), $n_s = n_s(r)$, and $T_s = T_s(r)$ are the charge, density, and temperature of species s , respectively, and the thermal transport coefficients are given by

$$L_{ij}^s = \frac{1}{q_s^2 \iota R_0 B_0^2} \sqrt{\frac{\pi m_s T_s^3}{8}} \int_0^\infty dK_s K_s^2 e^{-K_s} D_{ij}^*(K_s) h_i h_j, \quad (2)$$

with ι the rotational transform on a given flux surface, R_0 a reference major radius, m_s the mass of species s , $K_s = \frac{m_s v_s^2/2}{T_s} = \left(\frac{v_s}{v_{s,\text{thermal}}} \right)^2$, D_{ij}^* the monoenergetic transport coefficient evaluated for a given v_E^* , $h_1 = h_3 = 1$, and $h_2 = K_s$ [3]. While it may initially appear that $L_{11}^e/L_{11}^i \ll 1$ will always hold given the mass scaling in equation 2, it has been previously noted (to help explain the “impurity hole” phenomenon of the Large Helical Device [25, 26]) that sufficiently large L_{11}^e/L_{11}^i will cause $E_r > 0$ [12]. Optimized configurations have also recently been discovered by Beidler and coworkers with extremely small D_{11}^* at fuel-ion-relevant v_E^* and moderate values of ϵ_{eff} [27], leading to a large L_{11}^e/L_{11}^i and therefore a strong electron root in the core under reactor-relevant conditions. The theoretical foundations of this phenomenon are explored in more detail in recent work by Helander et al. [28].

The objective of our work is to follow the suggestion of reference [27] and optimize stellarator magnetic configurations to increase L_{11}^e/L_{11}^i . We control L_{11}^e through ϵ_{eff} and L_{11}^i through an array of D_{11}^* evaluated at fuel-ion-relevant v_E^* and $\nu^* \equiv R_0 \nu / \iota v$ (normalized collisionality) values. Monoenergetic transport coefficients should, in principle, provide a more general target than thermal transport coefficients because they are characteristic of a given magnetic field and do not depend on plasma profiles. Our transport optimizations are entirely neoclassical — because turbulence is often the dominant transport mechanism in optimized stellarators such as Wendelstein 7-X [29], the techniques presented here may only be useful when coupled with turbulence optimization techniques. Indeed, lowering the overall level of turbulence in a reactor

may well reduce the outward impurity flux provided by the turbulence and necessitate the presence of another impurity removal mechanism, such as an electron root. We note that large E'_r (and thus large $\mathbf{E}_r \times \mathbf{B}$ shear), which is common in electron root scenarios, may help reduce radial turbulent fluxes [30, 31]. Large E'_r , usually in the ion root region near the last closed flux surface, is known to allow access to improved confinement modes of operation somewhat similar to H-modes in tokamaks [9, 32, 33].

2. General Formulation

STELLOPT [34] is the primary optimization software used in this work. STELLOPT attempts to optimize finite- β MHD equilibria by minimizing an objective function of the form

$$\chi^2 = \sum_i \chi_i^2, \quad (3)$$

$$\chi_i^2 = \frac{(f_i - f_i^{\text{target}})^2}{\sigma_i^2}, \quad (4)$$

where f_i is any quantity that is callable by the STELLOPT routines, f_i^{target} is the desired value for f_i , and σ_i is a user-specified inverse weight. VMEC [35] is used as the MHD equilibrium solver in all cases. Differential evolution [36] and a Garabedian boundary representation [37] are utilized to find global minima more reliably except where noted in section 3.1.

The optimizations begin from a fixed-boundary configuration based on the W7-X high-mirror configuration [38] whose volume and on-axis magnetic field strength have been scaled to the reactor-relevant values of roughly 1756 m³ and 5 T, respectively [39]. Stellarator symmetry and five field periods are assumed for all optimizations. The initial value of β varies between optimizations as detailed in the next section. Zero bootstrap current is assumed during the MHD calculations within the optimization loop. The core feature of the optimizations is the minimization of an array of D_{11}^* with fuel-ion-relevant v_E^* and ν^* . The D_{11}^* values are calculated by DKES [40, 41], and a 3×3 array consisting of $|E_r|/v = \{5.00 \times 10^{-4}, 2.74 \times 10^{-3}, 1.50 \times 10^{-2}\}$ T and $\nu/v = \{2.50 \times 10^{-6}, 1.58 \times 10^{-5}, 1.00 \times 10^{-4}\}$ m⁻¹ is used. (These quantities, rather than their normalized counterparts, are specified as targets in STELLOPT.) The exact values of $|E_r|/v$ and ν/v seem relatively unimportant — the upper and lower values for each quantity are chosen to be approximately reactor-relevant bounds, and the middle values are the logarithmic means of the upper and lower values. Notably, modifications of B_0 , R_0 , and ι are relatively small in the optimizations, so explicitly targeting $|E_r|/v$ and ν/v rather than v_E^* and ν^* is acceptable. Even nearly doubling R_0 at the beginning of the Configuration 1 optimization (see section 3.1) made no noticeable difference to the output quality. In addition to D_{11}^* , we target $\epsilon_{\text{eff}} = 1\%$ (calculated by NEO [2]) in all optimizations except where noted in section 3.1. All neoclassical objectives are calculated for the $\rho = r/a = \{0.25, 0.5, 0.75\}$ flux surfaces. MHD objectives such

as plasma aspect ratio, elongation, and others are also included in the optimizations. Section 3 gives tabulated objective information for each optimization presented.

Once optimized, the transport characteristics of each configuration are analyzed using DKES and NTSS [42]. NTSS performs flux-surface-averaged, time-dependent transport calculations (including momentum correction techniques [43]) to determine self-consistent profiles for density, temperature, radial electric field, bootstrap current, and other quantities on 51 radial grid points for a given equilibrium. It should be emphasized that the equilibrium itself is not updated during the transport calculations, but NTSS calculates bootstrap current using the D_{31}^* database provided by DKES and updates the rotational transform profile by utilizing susceptance matrices [44]. Reactor volumes are rescaled to 1450 or 1900 m³ and on-axis magnetic field strengths are rescaled to 5 or 6 T to achieve an alpha power of 600 MW because this approximately corresponds to a 3 GWth reactor. (We note that the electron root is expected to be more difficult to achieve as the magnetic field strength increases [3, 31], which may need to be taken into account if our methods are used alongside those for turbulence optimization.) Deuterium and tritium density profiles are fixed with on-axis values for each in excess of 10¹⁹ m⁻³ and core gradients relatively flat in ρ — see figure 4 for details. NTSS uses the D-T cross-section to calculate the birth rate of alpha particles, which for simplicity are assumed to slow down on the flux surface of their birth. This determines the helium density, and quasineutrality then determines electron density. We assume there are no heavy impurities in the plasma. The temperature profiles for each species are initialized with roughly parabolic shapes in ρ , and the initial on-axis temperatures vary between analyses as described in the next section. A very simple turbulent transport model is included based on fits to W7-AS data. It takes the form [45]

$$Q_s^{\text{turb}} = -\chi_{\text{turb}} n_s T'_s, \quad (5)$$

$$\Gamma_s^{\text{turb}} = -D_{\text{turb}} n'_s, \quad (6)$$

where Q_s^{turb} is the radial energy flux of species s due to turbulence. Similarly to reference [27], we set $\chi_{\text{turb}} = 0.0065(P/\text{MW})^{3/4} / (n_s/10^{20} \text{ m}^{-3}) \text{ m}^2\text{s}^{-1}$ and $D_{\text{turb}} = 0.0003(P/\text{MW})^{3/4} / (n_s/10^{20} \text{ m}^{-3}) \text{ m}^2\text{s}^{-1}$ where $P = P_\alpha - P_{\text{Br}}$, P_α is the power deposited by fast ions, and P_{Br} is the power radiated due to Bremsstrahlung. No external heating is considered. NTSS determines the full profile of the radial electric field by solving a diffusion-like differential equation with hysteretic behavior [46] that minimizes the generalized heat production rate of the plasma [47]. This is necessary because the ambipolarity condition generally produces either one or three possible solutions for E_r [19, 48, 49] and a discontinuous E_r profile is nonphysical. In the case of three solutions, one is the ion root, one is the electron root, and one is an unstable root that is not physically realized. We choose the “diffusion coefficient” in the diffusion-like equation to be 2 m²/s such that the transition region from the electron root to the ion root is roughly 5 cm wide, which is reasonable in light of global neoclassical simulations [31]. Specifying a detailed startup scenario is beyond our scope, so we initialize NTSS runs by instructing the software to “select” the electron root solution if it exists. This situation is relevant

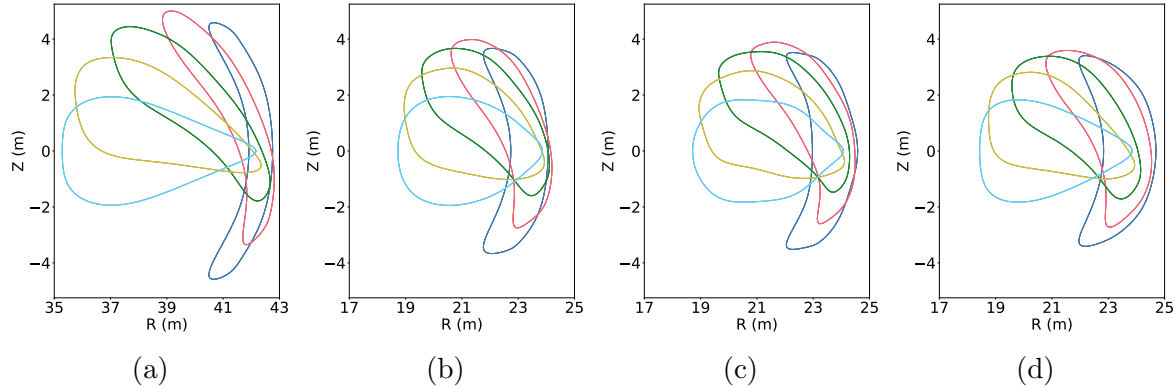


Figure 1: Toroidal cross-sections of the last closed flux surface equally spaced in the toroidal angle across one half-field-period for (a) Configuration 1 (section 3.1), (b) Configuration 2 (section 3.2), (c) Configuration 3 (section 3.3), and (d) scaled W7-X high-mirror.

Table 1: Plasma parameters of the configurations described in section 3. The “Initial P_α ” and “Initial P_{Br} ” entries refer to the alpha power and bremsstrahlung power, respectively, at the beginning of the NTSS simulation for the given configuration. The mirror ratio does not change throughout a simulation as the field strength is a user-specified parameter. All other entries refer to the end of the relevant NTSS simulation. τ_E is the energy confinement time, and τ_E^{ISS04} is calculated using the ISS04 scaling expression [50].

Quantity	Configuration 1	Configuration 2	Configuration 3
Mirror Ratio (%)	42.1	27.8	26.9
$\langle \beta \rangle_{\text{Vol}}$ (%)	4.94	4.43	3.14
Initial P_α (MW)	482.6	777.0	495.6
Final P_α (MW)	489.2	628.9	601.5
Initial P_{Br} (MW)	43.8	38.3	33.5
Final P_{Br} (MW)	72.7	73.7	72.7
τ_E (s)	$2.13 = 1.30\tau_E^{\text{ISS04}}$	$2.25 = 1.40\tau_E^{\text{ISS04}}$	$2.34 = 1.23\tau_E^{\text{ISS04}}$

for reactors that primarily utilize electron heating for startup. NTSS steps forward in time until it converges on a steady-state, self-consistent solution for the plasma profiles. We focus only on making the electron root realizable from a neoclassical standpoint and ensuring the optimized configurations can support the electron root during steady-state operation. (Configurations with insufficiently optimized ion confinement, such as scaled W7-X high-mirror, may be artificially seeded with an electron root during high-density operation but will transition to an ion root relatively quickly.)

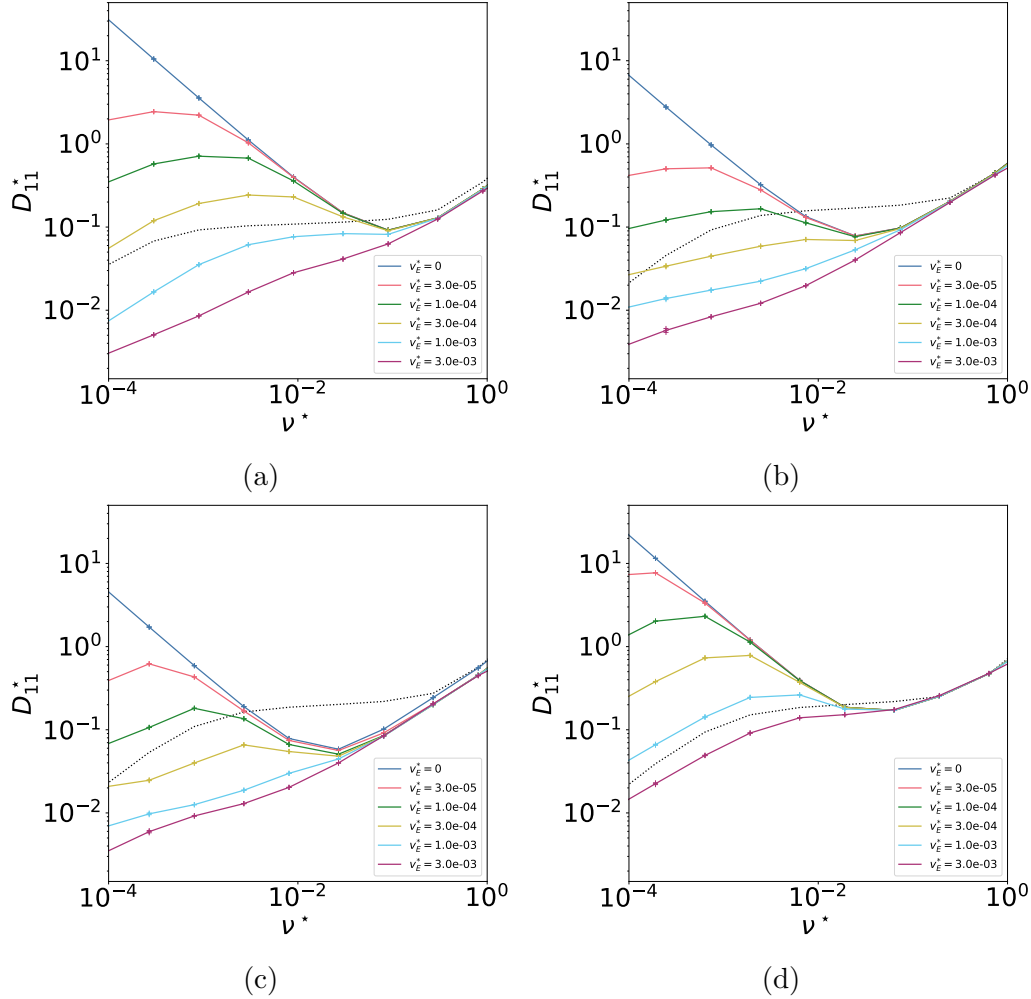


Figure 2: Scans of D_{11}^* versus ν^* with various v_E^* at $\rho \approx 0.35$ for (a) Configuration 1 (section 3.1), (b) Configuration 2 (section 3.2), (c) Configuration 3 (section 3.3), and (d) W7-X high-mirror. The upper and lower variational bounds on the D_{11}^* values are calculated by DKES and bracketed by the “+” symbols, but these “error bars” are too small to see in most cases. The dotted lines indicate D_{11}^* for a tokamak with the same aspect ratio, rotational transform, and (average) elongation as the given configuration for the same ρ . Note that the light blue and purple curves, roughly corresponding to fuel-ion-relevant v_E^* , are far more depressed in the optimized configurations (a – c) than in W7-X high-mirror. The characteristic gap between the (fuel-ion-relevant) high- v_E^* curves and (electron-relevant) $v_E^* = 0$ curves is also much larger in the optimized configurations than in W7-X high-mirror.

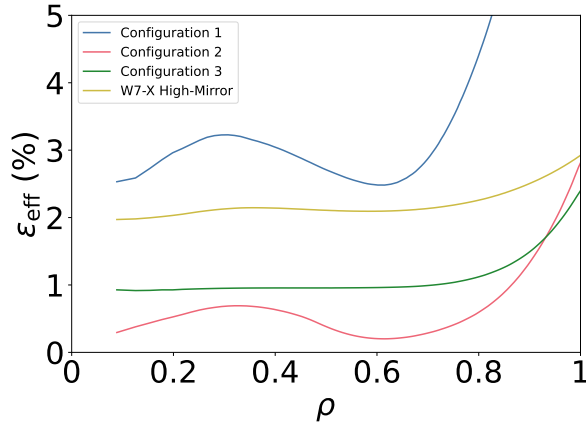


Figure 3: The geometric factor ϵ_{eff} for the configurations outlined in section 3 and W7-X high-mirror. These calculations are performed on the optimized equilibria without taking effects from the NTSS modeling (such as modifications to bootstrap current, β , etc.) into account. The large values of ϵ_{eff} in Configuration 1 as $\rho \rightarrow 1$ are likely numerical error — the high elongation of this configuration means many Boozer modes are required to fully describe the outermost surfaces, leading any codes that rely on Boozer coordinates to have questionable results there.

3. Results

3.1. Configuration 1

This optimization begins with a volume-averaged β of roughly 3.5%. The R_{00} Fourier component of the configuration is increased such that the initial aspect ratio is approximately 20. (Note that this increases the initial volume from the 1756 m³ quoted in section 2.) R_{00} is then removed from the optimization space to keep the aspect ratio roughly constant.

Unlike the other presented configurations, Configuration 1 is optimized in several stages. In stage 1, quasipoloidal (QP) symmetry is targeted. This was found to bring the configuration to a more favorable region of optimization space (to a point), likely because lowering the value of the Boozer B_{10} harmonic, the principle poloidal variation of B , tends to raise L_{11}^e/L_{11}^i [31]. In stage 2, the weight on QP symmetry is lowered in favor of targets for ϵ_{eff} and fuel-ion-relevant D_{11}^* . This is where the majority of the D_{11}^* optimization occurs. In stage 3, SFINCS [51] is used to “polish” the magnetic configuration by directly targeting thermal transport coefficients using differential evolution implemented in SciPy [52]. The optimizer is allowed to alter only the Fourier harmonics used by VMEC to describe the plasma, except for R_{00} . SFINCS is directed to perform calculations for electrons and a deuterium-tritium “hybrid” species. Density and temperature profiles are chosen to be generically reactor-relevant and consistent with the choice of β for the configuration. The radial electric field is arbitrarily set to 15 kV/m on each of the three considered flux surfaces. The L_{11}^e values from the

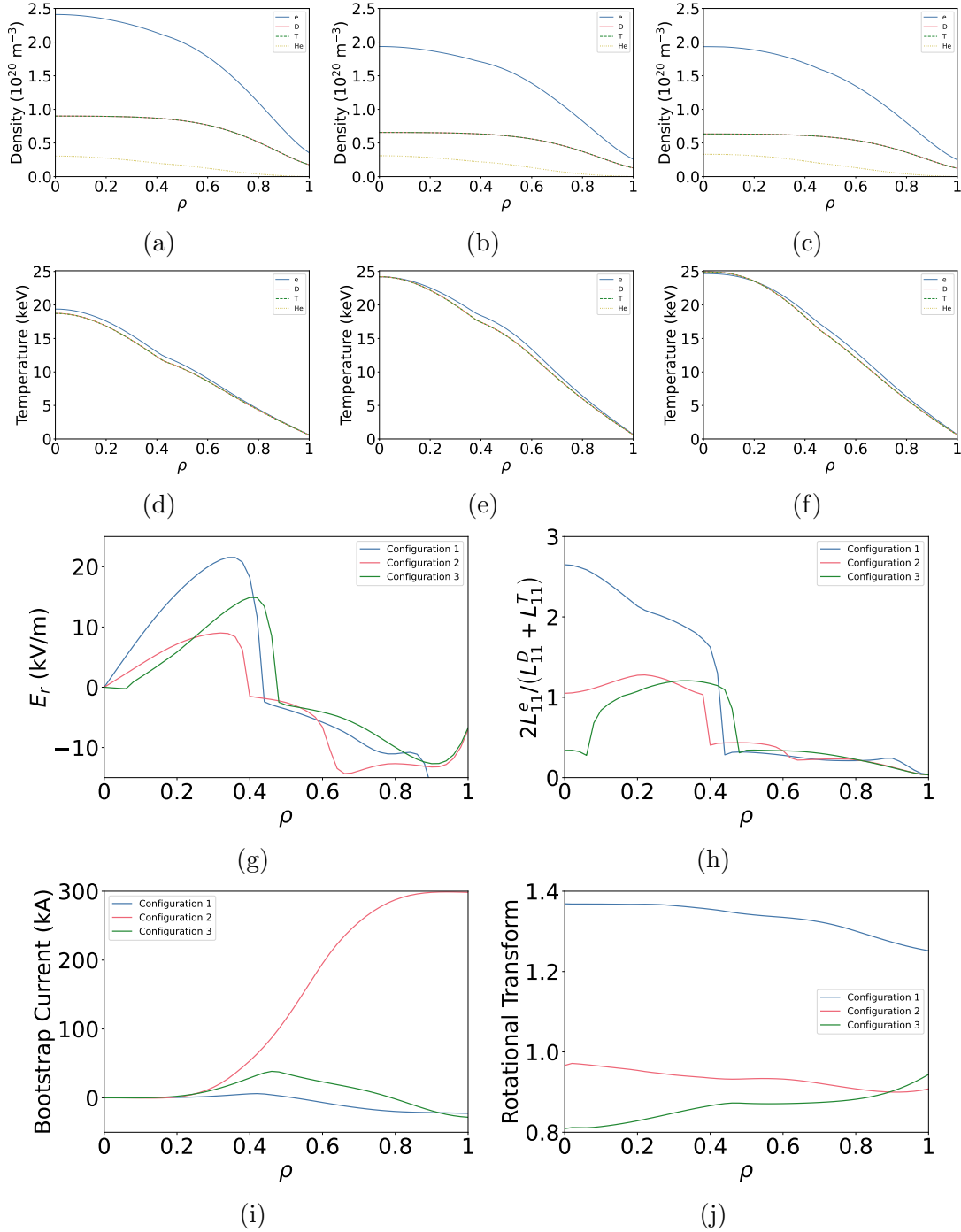


Figure 4: NTSS results for the steady-state density and temperature profiles of Configuration 1 (a+d), Configuration 2 (b+e), and Configuration 3 (c+f). The profiles of radial electric field (g), L_{11}^e/L_{11}^i (h), bootstrap current (i), and ι (j) are also included. Note that the results for Configuration 1 are suspect for $\rho \gtrsim 0.8$ — see the caption of figure 3 or the text in section 3.1 for an explanation.

Table 2: Optimization objectives used to produce Configuration 1 (section 3.1). Note that stages 1 and 2 are performed using STELLOPT, while SciPy optimization routines coupled with VMEC and SFINCS are used for stage 3. Note also that the L_{ij}^s values listed in stage 3 refer to the direct inputs for SFINCS, so they are unitless and have a different sign convention than the L_{ij}^s in equations 1 and 2. All targets except the aspect ratio are evaluated on the $\rho = \{0.25, 0.5, 0.75\}$ flux surfaces.

Objective	Target Value	Weight ($1/\sigma$)
Stage 1		
Aspect Ratio	20	10^1
QP Symmetry Breaking	0	10^2
Stage 2		
Aspect Ratio	20	10^1
QP Symmetry Breaking	0	10^1
ϵ_{eff}	1%	10^2
Fuel-Ion-Relevant D_{11}^*	0	10^2
Stage 3		
L_{11}^e	$\{-1.65 \times 10^{-4}, -5.16 \times 10^{-4}, -1.51 \times 10^{-3}\}$	10^0
L_{11}^i	0	10^0
L_{31}^e, L_{31}^i	0	10^0

end of stage 2 are used as targets in an attempt to hold radial electron transport roughly constant while driving L_{11}^i (and therefore radial ion transport) to zero. The bootstrap current thermal transport coefficients L_{31}^e and L_{31}^i are also targeted and driven toward zero to minimize the bootstrap current of the final configuration. Details of the targets used for this configuration can be found in table 2.

Figure 1 shows the cross-sections for Configuration 1, which are highly elongated (as expected when QP optimization is used). The elongation creates some difficulties in performing neoclassical calculations for the outer flux surfaces since the Boozer spectra required to describe these flux surfaces are very large — the numerical values of neoclassical quantities are likely imprecise for $\rho \gtrsim 0.8$ in Configuration 1. Figure 2 shows that in the core, the fuel-ion-relevant D_{11}^* are substantially reduced compared to W7-X high-mirror while the electron-relevant D_{11}^* are somewhat elevated. The latter point is corroborated by the ϵ_{eff} calculation shown in figure 3. These factors suggest this configuration will tend to have a relatively large L_{11}^e/L_{11}^i in the core. For the NTSS simulation shown in figure 4, the reactor volume is scaled to 1450 m^3 and the on-axis magnetic field is scaled to 5 T. The simulation is initialized with an electron core temperature of 15.60 keV and a fuel ion core temperature of 14.85 keV. The configuration has $L_{11}^e/L_{11}^i > 1$ for $0 \leq \rho \lesssim 0.4$ and consequently a strong electron root in this region. The bootstrap current is also small, and the configuration is coincidentally Mercier stable [53]. However, $\iota' < 0$ throughout, which makes the configuration

Table 3: Optimization objectives used to produce Configuration 2 (section 3.2). All targets except aspect ratio are evaluated on the $\rho = \{0.25, 0.5, 0.75\}$ flux surfaces.

Objective	Target Value	Weight ($1/\sigma$)
Aspect Ratio	10.89	10^1
ϵ_{eff}	1%	10^2
Fuel-Ion-Relevant D_{11}^*	0	10^2

vulnerable to neoclassical tearing modes [54], the aspect ratio is likely too large to be reactor-relevant, and the mirror ratio is very high (see table 1). Additionally, a final P_α of 600 MW could not be achieved due to the high elongation of the configuration causing an errant divergence in the electric field near the last closed flux surface when the reactor volume was raised above 1450 m³. While Configuration 1 is not a fully developed reactor design, it demonstrates the conceptual effectiveness of separately optimizing neoclassical ion transport (through D_{11}^*) and electron transport (through ϵ_{eff}).

3.2. Configuration 2

This optimization begins with a volume-averaged β of roughly 4.3%. The R_{00} Fourier harmonic is removed from the optimization space to prevent large changes in the aspect ratio through the course of the optimization. The philosophy of this optimization is to use a one-stage approach simpler than that of Configuration 1; consequently, only ϵ_{eff} , fuel-ion-relevant D_{11}^* , and aspect ratio are targeted, as can be seen in table 3. The first two targets are the most important and provide neoclassical optimization of the electrons and ions, respectively. The aspect ratio target is less important since R_{00} is not included in the optimization space — it serves only to keep the aspect ratio in the neighborhood of the initial configuration by regulating relatively small fluctuations due to higher boundary modes.

From figure 1, Configuration 2 is significantly less elongated than Configuration 1, with cross-sections much more similar to scaled W7-X high-mirror. However, as seen in figure 2, the reduction of fuel-ion-relevant D_{11}^* was even more substantial than in Configuration 1. From figure 3, ϵ_{eff} was somewhat lower than in W7-X throughout the volume, staying below the targeted 1% for $0 \leq \rho \lesssim 0.85$. This results in lower electron-relevant D_{11}^* values which compete with the small fuel-ion-relevant D_{11}^* to make L_{11}^e/L_{11}^i a bit smaller. For the NTSS calculations shown in figure 4, the reactor volume is scaled to 1900 m³ and the on-axis magnetic field is scaled to 5 T. The initial core electron temperature is 24.39 keV and the initial core fuel ion temperature is 23.21 keV. The figure shows that L_{11}^e/L_{11}^i is only slightly larger than 1 for Configuration 2 in the region $0 \leq \rho \lesssim 0.35$. An electron root appears in the same region with a peak E_r value roughly half that of Configuration 1. The electric field profile for $\rho \gtrsim 0.35$ has a somewhat unconventional shape, likely because the ϵ_{eff} profile is non-monotonic. While Configuration 2 has a favorable E_r profile and a lower mirror ratio than Configuration 1,

Table 4: Optimization objectives used to produce Configuration 3 (section 3.3). The neoclassical targets are evaluated on the $\rho = \{0.25, 0.5, 0.75\}$ flux surfaces. The rotational transform is evaluated on the $s = \rho^2 = \{0, 0.5, 1\}$ flux surfaces.

Objective	Target Value	Weight ($1/\sigma$)
Aspect Ratio	10.89	4×10^{-2}
Average Boundary Elongation	1.87	10^{-1}
Volume	1755.76 m^3	10^{-2}
ϵ_{eff}	1%	10^2
Fuel-Ion-Relevant D_{11}^*	0	10^2
Rotational Transform	$\{8.14 \times 10^{-1}, 8.70 \times 10^{-1}, 9.47 \times 10^{-1}\}$	10^0

it is Mercier unstable, has $\iota' < 0$ for most flux surfaces, and has a relatively large bootstrap current. It should also be noted that, as shown in table 1, the input power required to achieve the NTSS results shown is higher than the final output power of the configuration — while the displayed profiles are self-consistent, steady-state solutions to the transport equations, the system “relaxes” into them from profiles requiring extremely high input power. This suggests that while it is possible to obtain an electron root by optimizing fuel ion transport such that the ions (rather than electrons) are the rate-determining species for the radial neoclassical flux, it is very challenging to do so. The challenge may be attributed to the $\sqrt{m_s}$ factor in equation 2.

3.3. Configuration 3

This optimization begins with a volume-averaged β of roughly 5.0%. Unlike Configurations 1 and 2, R_{00} is included in the optimization space to allow for (small) changes to the aspect ratio, which is again one of the optimization targets. Volume and boundary elongation targets are also included in an attempt to prevent strong shaping like that found in Configuration 1. Values of these parameters from the initial configuration are used as targets. Rotational transform targets from the initial configuration are also included to help keep $\iota' > 0$ as this helps simultaneously improve MHD and neoclassical tearing mode stability. The same neoclassical targets were included as in section 3.2 and were the most important ingredients in the optimization. See table 4 for details.

Figure 1 shows that the last closed flux surface of Configuration 3 is very similar to that of Configuration 2, and figure 2 shows similar D_{11}^* optimization between Configurations 2 and 3. But unlike the other optimized configurations, Configuration 3 has an ϵ_{eff} of almost exactly 1% throughout the core. Because the fuel-ion-relevant D_{11}^* are well-optimized and $\epsilon_{\text{eff}} \approx 1\%$, we expect $L_{11}^e/L_{11}^i > 1$ in the core. For the NTSS simulation, the reactor volume is scaled to 1900 m^3 and the on-axis magnetic field is scaled to 6 T. The initial core electron temperature is 21.46 keV and the initial core fuel ion temperature is 18.57 keV. Figure 4 shows that L_{11}^e/L_{11}^i is slightly greater than 1

for $0.15 \lesssim \rho \lesssim 0.45$. Configuration 3 consequently has a weak ion root for $0 \lesssim \rho \lesssim 0.05$ and an electron root for $0.05 \lesssim \rho \lesssim 0.45$. The peak strength of E_r in the electron root region is intermediate between that of Configurations 1 and 2. The shape of the electric field profile in the ion root region is similar to that of W7-X for the same values of ρ . The difficulty in achieving an electron root deep in the core (which was observed several times in our testing) can perhaps be explained by the fact that flux surface shapes always tend to become elliptical as $\rho \rightarrow 0$ [55]. Confinement (omnigenity) of electrons places constraints on the contours of B_{\min} , whereas confinement of fuel ions places constraints on the contours of B_{\max} [56]. If cross-sections are almost purely elliptical, as is the case near the magnetic axis, it is difficult to optimize the magnetic field such that the latter constraints are (approximately) respected while the former are violated, which is necessary for the production of an electron root. Far from the axis, where there is more freedom to shape flux surfaces, this task becomes easier. In addition to an electron root in most of the core, Configuration 3 has a relatively small bootstrap current, nearly monotonically positive magnetic shear, and a reasonable power balance (see table 1). However, it is Mercier unstable. Again, we find that optimizing neoclassical ion and electron transport separately enables the production of a steady-state electron root at reactor-relevant collisionalities, but the task is challenging.

4. Conclusions

We have shown through several examples that neoclassical electron and fuel ion transport can be optimized separately to raise the ratio L_{11}^e/L_{11}^i and produce an outward-pointing ambipolar electric field in the core under reactor-relevant conditions. These configurations are expected to expel heavy impurities from the core during steady-state operation. However, we were unable to generate any completely satisfactory configurations despite substantial effort. One configuration we produced had stronger fuel-ion-relevant D_{11}^* suppression than any of the configurations presented here, but effects related to the slope of the D_{11}^* vs ν^* curves (like those in figure 2) and the resonant electric field prevented an electron root from being realized. Further development is needed before the approach outlined in this work is ready for mainstream use.

A possible extension of this work involves coupling a modern, fast neoclassical transport code such as KNOSOS [57, 58] to a modern optimization framework such as SIMSOPT [59] and performing optimizations similar to those presented in section 3. This will likely avoid some of the numerical difficulties we encountered while attempting to improve the optimizations and allow for consideration of additional neoclassical effects. Notably, KNOSOS includes the tangential magnetic drifts (unlike DKES), which can be substantial for some configurations [60] and alter the confinement of fuel and impurity ions [61]. The tangential drifts can also make the electron root more difficult to achieve in maximum- J configurations [62]. Because the maximum- J property helps mitigate turbulence [63], it may be a useful optimization target for future devices. A code that takes the tangential drifts into account would therefore

be helpful if an electron root is to be targeted as well. Due to its speed, KNOSOS can also calculate thermal transport coefficients very quickly. The final stage of the optimization in section 3.1 successfully improved a configuration with optimized monoenergetic transport coefficients by targeting thermal transport coefficients using the (relatively slow) SFINCS code. This suggests that targeting thermal transport coefficients throughout the optimization may be helpful — Lascas Neto and coworkers [64] have recently used SFINCS to do so and obtained promising results.

Another possible extension of this work involves developing a more theoretical approach to ensuring excellent neoclassical confinement of fuel ions and moderate confinement of electrons. Helander and coworkers [28] exploited the fact that in the formulation of omnigenity, there are separate conditions for zero average radial drift of marginally trapped particles (which pertains to fuel ions) and deeply trapped particles (which pertains to electrons). They derive an expression that allows the former conditions to be satisfied while the latter are violated and optimize a stellarator configuration using this expression as an objective. We suggest that further refinement of the analytical proxy, or perhaps a blend of the analytical and computational approaches, may provide the most reliable results for future stellarator optimization efforts.

Once a more reliable algorithm for electron root optimization has been devised, it will likely be beneficial to include a reasonably sophisticated turbulence model in the post-optimization transport simulations. This will indicate whether the large E'_r in the core reduces turbulent fluxes. Recently devised simulation frameworks [65] should provide this capability. Exploring the Pareto fronts between the electron root objective and other physics and engineering objectives will also be helpful for future design studies.

Acknowledgments

We thank Stefan Buller, José Luis Velasco, Matt Landreman, Per Helander, Michael Drevlak, Alan Goodman, Eduardo Lascas Neto, Eduardo Rodríguez, and Katia Camacho Mata for their insights and assistance.

This work was supported by a Fulbright grant from the German-American Fulbright Commission. This material is based upon work supported by the U.S. Department of Energy, Office of Science, Office of Advanced Scientific Computing Research, under Award Number DE-SC0024386. This work has been carried out within the framework of the EUROfusion Consortium, funded by the European Union via the Euratom Research and Training Programme (Grant Agreement No. 101052200 – EUROfusion). Views and opinions expressed are however those of the author(s) only and do not necessarily reflect those of the European Union or the European Commission. Neither the European Union nor the European Commission can be held responsible for them. Computations were performed on the Cobra and Raven HPC systems at the Max Planck Computing and Data Facility.

References

- [1] Per Helander. Theory of plasma confinement in non-axisymmetric magnetic fields. *Reports on Progress in Physics*, 81(9):087001, 2018.
- [2] V. V. Nemov, S. V. Kasilov, W. Kernbichler, and M. F. Heyn. Evaluation of $1/\nu$ neoclassical transport in stellarators. *Physics of Plasmas*, 6(12):4622–4632, 1999.
- [3] C. D. Beidler, K. Allmaier, M. Yu Isaev, S. V. Kasilov, W. Kernbichler, G. O. Leitold, H. Maaßberg, D. R. Mikkelsen, S. Murakami, M. Schmidt, D. A. Spong, V. Tribaldos, and A. Wakasa. Benchmarking of the mono-energetic transport coefficients - Results from the International Collaboration on Neoclassical Transport in Stellarators (ICNTS). *Nuclear Fusion*, 51(7):076001, 2011.
- [4] Darwin D.-M. Ho and Russel M. Kulsrud. Neoclassical Transport in Stellarators. *Physics of Fluids*, 30(2):442–461, 1987.
- [5] C. D. Beidler, E. Harmeyer, F. Herrnegger, Yu. Igitkhanov, A. Kendl, J. Kisslinger, Ya. I. Kolesnichenko, V. V. Lutsenko, C. Nührenberg, I. Sidorenko, E. Strumberger, H. Wobig, and Yu. V. Yakovenko. The Helias reactor HSR4/18. *Nuclear Fusion*, 41(12):1759–1766, 2001.
- [6] L. P. Ku, P. R. Garabedian, J. Lyon, A. Turnbull, A. Grossman, T. K. Mau, M. Zarnstorff, and the ARIES Team. Physics Design for ARIES-CS. *Fusion Science and Technology*, 54(3):673–693, 2008.
- [7] P. H. Rutherford. Impurity transport in the Pfirsch-Schlüter regime. *The Physics of Fluids*, 17(9):1782–1784, 1974.
- [8] W VII-A Team and NI Group. Impurity transport in the wendelstein VII-A stellarator. *Nuclear Fusion*, 25(11):1593–1609, 1985.
- [9] M. Hirsch, J. Baldzuhn, C. Beidler, R. Brakel, R. Burhenn, A. Dinklage, H. Ehmler, M. Endler, V. Erckmann, Y. Feng, J. Geiger, L. Giannone, G. Grieger, P. Grigull, H.-J. Hartfuß, D. Hartmann, R. Jaenicke, R. König, H. P. Laqua, H. Maaßberg, K. McCormick, F. Sardei, E. Speth, U. Stroth, F. Wagner, A. Weller, A. Werner, H. Wobig, S. Zoleznik, and the W7-AS Team. Major results from the stellarator Wendelstein 7-AS. *Plasma Physics and Controlled Fusion*, 50(5):053001, 2008.
- [10] J. M. García-Regaña, R. Kleiber, C. D. Beidler, Y. Turkin, H. Maaßberg, and P. Helander. On neoclassical impurity transport in stellarator geometry. *Plasma Physics and Controlled Fusion*, 55(7):074008, 2013.
- [11] A. Mollén, M. Landreman, H. M. Smith, S. Braun, and P. Helander. Impurities in a non-axisymmetric plasma: Transport and effect on bootstrap current. *Physics of Plasmas*, 22(11):112508, 2015.
- [12] J. L. Velasco, I. Calvo, S. Satake, A. Alonso, M. Nunami, M. Yokoyama, M. Sato, T. Estrada, J. M. Fontdecaba, M. Liniers, K. J. McCarthy, F. Medina, B. Ph Van Milligen, M. Ochando, F. Parra, H. Sugama, and A. Zhezhera. Moderation of neoclassical impurity accumulation in high temperature plasmas of helical devices. *Nuclear Fusion*, 57(1):016016, 2017.

- [13] P. Helander, S. L. Newton, A. Mollén, and H. M. Smith. Impurity Transport in a Mixed-Collisionality Stellarator Plasma. *Physical Review Letters*, 118(15):155002, 2017.
- [14] J. M. García-Regaña, C. D. Beidler, R. Kleiber, P. Helander, A. Mollén, J. A. Alonso, M. Landreman, H. Maaßberg, H. M. Smith, Y. Turkin, and J. L. Velasco. Electrostatic potential variation on the flux surface and its impact on impurity transport. *Nuclear Fusion*, 57(5):056004, 2017.
- [15] S. Buller, H. M. Smith, P. Helander, A. Mollén, S. L. Newton, and I. Pusztai. Collisional transport of impurities with flux-surface varying density in stellarators. *Journal of Plasma Physics*, 84(4):905840409, 2018.
- [16] Iván Calvo, Felix I. Parra, José Luis Velasco, J. Arturo Alonso, and J. M. García-Regaña. Stellarator impurity flux driven by electric fields tangent to magnetic surfaces. *Nuclear Fusion*, 58(12):124005, 2018.
- [17] A. Mollén, M. Landreman, H. M. Smith, J. M. García-Regaña, and M. Nunami. Flux-surface variations of the electrostatic potential in stellarators: impact on the radial electric field and neoclassical impurity transport. *Plasma Physics and Controlled Fusion*, 60(8):84001, 2018.
- [18] S. Buller, H. M. Smith, and A. Mollén. Recent progress on neoclassical impurity transport in stellarators with implications for a stellarator reactor. *Plasma Physics and Controlled Fusion*, 63(5):054003, 2021.
- [19] Harry E. Mynick. Effect of collisionless detrapping on nonaxisymmetric transport in a stellarator with radial electric field. *The Physics of Fluids*, 26(9):2609–2615, 1983.
- [20] D. E. Hastings, W. A. Houlberg, and K. C. Shaing. The ambipolar electric field in stellarators. *Nuclear Fusion*, 25(4):445–454, 1985.
- [21] H. Maaßberg, C. D. Beidler, U. Gasparino, M. Romé, K. S. Dyabilin, N. B. Marushchenko, and S. Murakami. The neoclassical “electron root” feature in the Wendelstein-7-AS stellarator. *Physics of Plasmas*, 7(1):295–311, 2000.
- [22] M. Yokoyama, H. Maaberg, C. D. Beidler, V. Tribaldos, K. Ida, T. Estrada, F. Castejon, A. Fujisawa, T. Minami, T. Shimozuma, Y. Takeiri, A. Dinklage, S. Murakami, and H. Yamada. Core electron-root confinement (CERC) in helical plasmas. *Nuclear Fusion*, 47(9):1213–1219, 2007.
- [23] T. Klinger, A. Alonso, S. Bozhenkov, R. Burhenn, A. Dinklage, G. Fuchert, J. Geiger, O. Grulke, A. Langenberg, M. Hirsch, G. Kocsis, J. Knauer, A. Krämer-Flecken, H. Laqua, S. Lazerson, M. Landreman, H. Maaßberg, S. Marsen, M. Otte, N. Pablant, E. Pasch, K. Rahbarnia, T. Stange, T. Szepesi, H. Thomsen, P. Traverso, J. L. Velasco, T. Wauters, G. Weir, T. Windisch, and The Wendelstein 7-X Team. Performance and properties of the first plasmas of Wendelstein 7-X. *Plasma Physics and Controlled Fusion*, 59(1):014018, 2017.

- [24] N. A. Pablant, A. Langenberg, A. Alonso, C. D. Beidler, M. Bitter, S. Bozhenkov, R. Burhenn, M. Beurskens, L. Delgado-Aparicio, A. Dinklage, G. Fuchert, D. Gates, J. Geiger, K. W. Hill, U. Höfel, M. Hirsch, J. Knauer, A. Krämer-Flecken, M. Landreman, S. Lazerson, H. Maaßberg, O. Marchuk, S. Massidda, G. H. Neilson, E. Pasch, S. Satake, J. Svennson, P. Traverso, Y. Turkin, P. Valson, J. L. Velasco, G. Weir, T. Windisch, R. C. Wolf, M. Yokoyama, D. Zhang, and the W7-X Team. Core radial electric field and transport in Wendelstein 7-X plasmas. *Physics of Plasmas*, 25(2):022508, 2018.
- [25] M. Yoshinuma, K. Ida, M. Yokoyama, M. Osakabe, K. Nagaoka, S. Morita, M. Goto, N. Tamura, C. Suzuki, S. Yoshimura, H. Funaba, Y. Takeiri, K. Ikeda, K. Tsumori, and O. Kaneko. Observation of an impurity hole in the Large Helical Device. *Nuclear Fusion*, 49(6):062002, 2009.
- [26] K. Ida, M. Yoshinuma, M. Osakabe, K. Nagaoka, M. Yokoyama, H. Funaba, C. Suzuki, T. Ido, A. Shimizu, I. Murakami, N. Tamura, H. Kasahara, Y. Takeiri, K. Ikeda, K. Tsumori, O. Kaneko, S. Morita, M. Goto, K. Tanaka, K. Narihara, T. Minami, I. Yamada, and the LHD Experimental Group. Observation of an impurity hole in a plasma with an ion internal transport barrier in the Large Helical Device. *Physics of Plasmas*, 16(5):056111, 2009.
- [27] C. D. Beidler, M. Drevlak, J. Geiger, P. Helander, H. M. Smith, and Y. Turkin. Reduction of neoclassical bulk-ion transport to avoid helium-ash retention in stellarator reactors. Submitted to *Nuclear Fusion*, 2024.
- [28] Per Helander, Alan G. Goodman, Craig D. Beidler, Michal Kuczyński, and Håkan M. Smith. Optimised stellarators with a positive radial electric field, May 2024. arXiv:2405.07085.
- [29] D. Carralero, T. Estrada, E. Maragkoudakis, T. Windisch, J. A. Alonso, M. Beurskens, S. Bozhenkov, I. Calvo, H. Damm, O. Ford, G. Fuchert, J. M. García-Regaña, N. Pablant, E. Sánchez, E. Pasch, J. L. Velasco, and the Wendelstein 7-X Team. An experimental characterization of core turbulence regimes in Wendelstein 7-X. *Nuclear Fusion*, 61(9):096015, 2021.
- [30] P. W. Terry. Suppression of turbulence and transport by sheared flow. *Reviews of Modern Physics*, 72(1):109–165, 2000.
- [31] M. D. Kuczyński, R. Kleiber, H. M. Smith, C. D. Beidler, M. Borchardt, J. Geiger, and P. Helander. Self-consistent, global, neoclassical radial-electric-field calculations of electron-ion-root transitions in the W7-X stellarator. *Nuclear Fusion*, 64(4):046023, 2024.
- [32] F. Wagner. A quarter-century of H-mode studies. *Plasma Physics and Controlled Fusion*, 49(12B):B1–B33, 2007.
- [33] T. Estrada, T. Happel, L. Eliseev, D. López-Bruna, E. Ascasíbar, E. Blanco, L. Cupido, J. M. Fontdecaba, C. Hidalgo, R. Jiménez-Gómez, L. Krupnik, M. Liniers, M. E. Manso, K. J. McCarthy, F. Medina, A. Melnikov, B. van Milligen,

M. A. Ochando, I. Pastor, M. A. Pedrosa, F. L. Tabarés, D. Tafalla, and the TJ-II Team. Sheared flows and transition to improved confinement regime in the TJ-II stellarator. *Plasma Physics and Controlled Fusion*, 51(12):124015, 2009.

[34] Samuel Lazerson, John Schmitt, Zhu Caoxiang, Joshua Breslau, and All STELLOPT Developers. STELLOPT, 2020.

[35] S. P. Hirshman and J. C. Whitson. Steepest-descent moment method for three-dimensional magnetohydrodynamic equilibria. *The Physics of Fluids*, 26(12):3553–3568, 1983.

[36] Rainer Storn and Kenneth Price. Differential Evolution – A Simple and Efficient Heuristic for Global Optimization over Continuous Spaces. *Journal of Global Optimization*, 11:341–359, 1997.

[37] Paul R. Garabedian. Quasi-axially symmetric stellarators. *Proceedings of the National Academy of Sciences*, 95(17):9732–9737, 1998.

[38] A. Dinklage, C. D. Beidler, P. Helander, G. Fuchert, H. Maaßberg, K. Rahbarnia, T. Sunn Pedersen, Y. Turkin, R. C. Wolf, T. Andreeva, S. Bozhenkov, B. Buttenschön, Y. Feng, J. Geiger, M. Hirsch, U. Höfel, M. Jakubowski, T. Klinger, J. Knauer, A. Langenberg, H. P. Laqua, N. Marushchenko, A. Mollén, U. Neuner, H. Niemann, E. Pasch, L. Rudischhauser, H. M. Smith, T. Stange, G. Weir, T. Windisch, D. Zhang, S. Äkäslompolo, A. Ali, J. Alcason Bellosa, P. Aleynikov, K. Aleynikova, J. Baldzuhn, M. Banduch, C. Beidler, A. Benndorf, M. Beurskens, C. Biedermann, D. Birus, M. Blatzheim, T. Bluhm, D. Böckenhoff, M. Borchardt, H. S. Bosch, L. G. Böttger, R. Brakel, Ch Brandt, T. Bräuer, H. Braune, K. J. Brunner, B. Brünner, R. Burhenn, R. Bussahn, V. Bykov, A. Card, A. Carls, S. Degenkolbe, C. P. Dhard, M. Drevlak, P. Drewelow, A. Dudek, P. van Eeten, G. Ehrke, M. Endler, E. Erckmann, N. Fahrenkamp, J. H. Feist, J. Fellinger, O. Ford, B. Geiger, D. Gradic, M. Grahl, H. Grote, O. Grulke, P. Hacker, K. Hammond, H. J. Hartfuß, D. Hartmann, D. Hathiramani, B. Hein, S. Henneberg, C. Hennig, H. Hölbe, A. Hölting, H. Jenzsch, J. P. Kallmeyer, U. Kamionka, C. Killer, R. Kleiber, A. Könies, M. Köppen, R. König, P. Kornejew, R. Krampitz, J. Krom, M. Krychowiak, G. Kühner, S. Kwak, R. Laube, S. Lazerson, L. Lewerentz, J. F. Lobsien, J. Loizu Cisquella, A. Lorenz, S. Marsen, M. Marushchenko, P. McNeely, O. Mishchenko, B. Missal, T. Mönnich, D. Moseev, M. Nagel, D. Naujoks, C. Nührenberg, J. Nührenberg, J. W. Oosterbeek, M. Otte, N. Panadero, A. Pavone, V. Perseo, D. Pilopp, S. Pingel, G. Plunk, A. Puig Sitjes, F. Purps, J. Riemann, K. Riße, A. Rodatos, P. Rong, K. Rummel, T. Rummel, A. Runov, N. Rust, J. Schacht, F. Schauer, G. Schlisio, M. Schneider, W. Schneider, M. Schröder, T. Schröder, R. Schroeder, B. Shanahan, P. Sinha, C. Slaby, H. Smith, A. Spring, U. Stridde, J. Svensson, H. Thomsen, H. Trimino Mora, I. Vakulchik, S. Valet, H. Viebke, R. Vilbrandt, F. Warmer, L. Wegener, T. Wegner, J. Wendorf, U. Wenzel, F. Wilde, E. Winkler, P. Xanthopoulos, J. Zhu, A. Zocco, F. Köster, A. Alonso, E. Ascasibar, E. Blanco, I. Calvo, A. Cappa, F. Castejon, A. de la

Pena, H. Esteban, T. Estrada, J. Fontdecaba, J. García Regaña, M. Garcia-Munoz, C. Guerard, J. Hernandez Sanchez, C. Hidalgo, K. McCarthy, L. Pacios Rodriguez, N. Panadero Alvarez, M. Sanchez, B. Milligen, J. L. Velasco, B. Blackwell, J. Howard, A. Wright, A. Czarnecka, M. Kubkowska, W. Figacz, T. Fornal, A. Galkowski, M. Gruca, S. Jablonski, J. Kacmarczyk, N. Krawczyk, G. Pelka, L. Ryc, M. Scholz, J. Wolowski, F. Effenberg, O. Schmitz, T. Barbui, H. Frerichs, J. Green, T. Kremeyer, L. Stephey, V. Winters, G. Kocsis, T. Szepesi, G. Anda, G. Cseh, T. Ilkei, G. Náfrádi, S. Récsei, V. Szabó, T. Szabolics, Z. Szökefalvi-Nagy, S. Tulipán, S. Zoletnik, A. Krämer-Flecken, J. Assmann, W. Behr, O. Bertuch, W. Biel, V. Borsuk, S. Brezinsek, Y. Cai, A. Charl, G. Czymek, P. Denner, T. Dittmar, M. Dostal, Ph Drews, A. Freund, Y. Gao, N. Gierse, X. Han, F. Harberts, K. P. Hollfeld, D. Höschen, M. Knaup, A. Knieps, R. Koslowski, Th Krings, M. Lennartz, Y. Liang, Ch Linsmeier, S. Liu, O. Marchuk, Ph Mertens, O. Neubauer, G. Offermanns, A. Panin, M. Rack, D. Reiter, G. Satheeswaran, H. Schmitz, B. Schweer, A. Terra, J. Thomas, B. Unterberg, M. Vervier, E. Wang, N. Wang, Y. Wei, N. Pablant, P. Bolgert, D. Gates, P. Heitzenroeder, B. Israeli, S. Langish, D. Loesser, M. Mardenfeld, D. Mikkelsen, J. Mittelstaedt, H. Neilson, A. Reiman, M. Sibilia, P. Titus, M. Zarnstorff, H. Zhang, G. A. Wurden, G. Wurden, M. Landreman, F. Durodie, A. Goriaev, Y. Kazakov, J. Ongena, M. Vergote, T. Wauters, R. Alzbutas, G. Dundulis, T. Kaliatka, R. Karalevicius, M. Povilaitis, S. Rimkevicius, E. Urbonavicius, S. G. Baek, J. Maisano-Brown, J. Terry, M. Barlak, G. Gawlik, J. Jagielski, R. Koziol, P. Kraszewsk, K. Baumann, G. Dammertz, W. H. Fietz, G. Gantenbein, M. Huber, H. Hunger, S. Illy, J. Jelonnek, Th Kobarg, R. Lang, W. Leonhardt, M. Losert, A. Meier, D. Mellein, D. Papenfuß, A. Samartsev, T. Scherer, A. Schlaich, W. Spiess, M. Thumm, S. Wadle, J. Weggen, J. Boscary, M. Czerwinski, B. Heinemann, P. Junghans, B. Mendelevitch, R. Nocentini, S. Obermayer, G. Orozco, R. Riedl, P. Scholz, R. Stadler, B. Standley, J. Tretter, A. Vorkörper, M. Zilker, I. Abramovic, H. Brand, S. Paqay, J. Proll, B. Cannas, F. Pisano, L. Carraro, M. Zuin, B. Carvalho, A. da Silva, H. Fernandes, B. Goncalves, F. Chernyshev, M. Cianciosa, M. J. Cole, J. H. Harris, J. Lore, A. Lumsdaine, D. A. Spong, R. Citarella, V. Giannella, Ciupiński, G. Krzesinski, P. Marek, G. Claps, F. Cordella, A. Czermak, L. Haiduk, Z. Sulek, K. Czerski, A. da Molin, D. Ennis, D. Maurer, J. Schmitt, P. Traverso, M. Führer, T. Funaba, X. Huang, K. Ida, H. Kasahara, N. Kenmochi, S. Masuzaki, T. Morisaki, K. Ogawa, B. Peterson, S. Ryosuke, R. Sakamoto, S. Satake, Y. Suzuki, N. Tamura, K. Toi, H. Tsuchiya, T. Tsujimura, H. Yamada, I. Yamada, R. Yasuhara, M. Yokoyama, A. Gogoleva, L. Vela, A. Grosman, M. Houry, V. Moncada, T. Ngo, S. Renard, J. M. Travere, V. Huber, D. Kinna, S. Schmuck, C. P. von Thun, M. Turnyanskiy, A. Ivanov, A. Khilchenko, I. V. Shikhovtsev, W. Kasperek, M. Krämer, C. Lechte, R. Munk, B. Plaum, F. Remppel, H. Röhlinger, B. Roth, K. H. Schlüter, S. Wolf, A. Zeitler, M. Keunecke, F. Köchl, Y. Kolesnichenko, V. Lutsenko, J. Koshurinov, L. Lubyako, I. Ksiazek, F. Musielok,

E. Pawelec, T. Kurki-Suonio, S. Sipilä, A. Lücke, A. Pieper, H. Schumacher, B. Wiegel, A. Zimbal, T. Mizuuchi, S. Murakami, F. Sano, W. Pan, X. Peng, J. Preinhaelter, J. Urban, J. Zajac, M. E. Puiatti, M. Romé, H. J. Roscher, J. Skodzik, D. Timmermann, M. Stoneking, N. Vianello, and R. Schrittwieser. Magnetic configuration effects on the Wendelstein 7-X stellarator. *Nature Physics*, 14(8):855–860, 2018.

[39] Samuel A. Lazerson, Alexandra Leviness, and Jorrit Lion. Simulating fusion alpha heating in a stellarator reactor. *Plasma Physics and Controlled Fusion*, 63(12):125033, 2021.

[40] S. P. Hirshman, K. C. Shaing, W. I. van Rij, C. O. Beasley, and E. C. Crume. Plasma transport coefficients for nonsymmetric toroidal confinement systems. *Physics of Fluids*, 29(9):2951–2959, 1986.

[41] W. I. van Rij and S. P. Hirshman. Variational bounds for transport coefficients in three-dimensional toroidal plasmas. *Physics of Fluids B*, 1(3):563–569, 1989.

[42] Y. Turkin, H. Maassberg, C. D. Beidler, J. Geiger, and N. B. Marushchenko. Current control by ECCD for W7-X. *Fusion Science and Technology*, 50(3):387–394, 2006.

[43] H. Maaßberg, C. D. Beidler, and Y. Turkin. Momentum correction techniques for neoclassical transport in stellarators. *Physics of Plasmas*, 16(7):072504, 2009.

[44] P. I. Strand and W. A. Houlberg. Magnetic flux evolution in highly shaped plasmas. *Physics of Plasmas*, 8(6):2782–2792, 2001.

[45] H. Ringler, U. Gasparino, G. Kühner, E. Maaßberg, H. Renner, F. Sardei, the W VII-AS Team, and the NBI Team. Confinement studies on the Wendelstein VII-AS stellarator. *Plasma Physics and Controlled Fusion*, 32(11):933–948, 1990.

[46] D. E. Hastings. A differential equation for the ambipolar electric field in a multiple-helicity torsatron. *Physics of Fluids*, 28(1):334–337, 1985.

[47] K. C. Shaing. Stability of the radial electric field in a nonaxisymmetric torus. *Physics of Fluids*, 27(7):1567–1572, 1984.

[48] E. F. Jaeger, D. A. Spong, and C. L. Hedrick. Neoclassical Transportation in the ELMO Bumpy Torus. *Physical Review Letters*, 40(13):866–869, 1978.

[49] D. E. Hastings. Bifurcation phenomena and the radial electric field in a nonaxisymmetric plasma. *Physics of Fluids*, 29(2):536–543, 1986.

[50] H. Yamada, J. H. Harris, A. Dinklage, E. Ascasibar, F. Sano, S. Okamura, J. Talmadge, U. Stroth, A. Kus, S. Murakami, M. Yokoyama, C. D. Beidler, V. Tribaldos, K. Y. Watanabe, and Y. Suzuki. Characterization of energy confinement in net-current free plasmas using the extended International Stellarator Database. *Nuclear Fusion*, 45(12):1684–1693, 2005.

[51] M. Landreman, H. M. Smith, A. Mollén, and P. Helander. Comparison of particle trajectories and collision operators for collisional transport in nonaxisymmetric plasmas. *Physics of Plasmas*, 21(4):042503, 2014.

[52] Pauli Virtanen, Ralf Gommers, Travis E. Oliphant, Matt Haberland, Tyler Reddy, David Cournapeau, Evgeni Burovski, Pearu Peterson, Warren Weckesser, Jonathan Bright, Stéfan J. van der Walt, Matthew Brett, Joshua Wilson, K. Jarrod Millman, Nikolay Mayorov, Andrew R. J. Nelson, Eric Jones, Robert Kern, Eric Larson, C J Carey, İlhan Polat, Yu Feng, Eric W. Moore, Jake VanderPlas, Denis Laxalde, Josef Perktold, Robert Cimrman, Ian Henriksen, E. A. Quintero, Charles R. Harris, Anne M. Archibald, Antônio H. Ribeiro, Fabian Pedregosa, Paul Van Mulbregt, SciPy 1.0 Contributors, Aditya Vijaykumar, Alessandro Pietro Bardelli, Alex Rothberg, Andreas Hilboll, Andreas Kloeckner, Anthony Scopatz, Antony Lee, Ariel Rokem, C. Nathan Woods, Chad Fulton, Charles Masson, Christian Häggström, Clark Fitzgerald, David A. Nicholson, David R. Hagen, Dmitrii V. Pasechnik, Emanuele Olivetti, Eric Martin, Eric Wieser, Fabrice Silva, Felix Lenders, Florian Wilhelm, G. Young, Gavin A. Price, Gert-Ludwig Ingold, Gregory E. Allen, Gregory R. Lee, Hervé Audren, Irvin Probst, Jörg P. Dietrich, Jacob Silterra, James T Webber, Janko Slavić, Joel Nothman, Johannes Buchner, Johannes Kulick, Johannes L. Schönberger, José Vinícius De Miranda Cardoso, Joscha Reimer, Joseph Harrington, Juan Luis Cano Rodríguez, Juan Nunez-Iglesias, Justin Kuczynski, Kevin Tritz, Martin Thoma, Matthew Newville, Matthias Kümmerer, Maximilian Bolingbroke, Michael Tartre, Mikhail Pak, Nathaniel J. Smith, Nikolai Nowaczyk, Nikolay Shebanov, Oleksandr Pavlyk, Per A. Brodtkorb, Perry Lee, Robert T. McGibbon, Roman Feldbauer, Sam Lewis, Sam Tygier, Scott Sievert, Sebastiano Vigna, Stefan Peterson, Surhud More, Tadeusz Pudlik, Takuya Oshima, Thomas J. Pingel, Thomas P. Robitaille, Thomas Spura, Thouis R. Jones, Tim Cera, Tim Leslie, Tiziano Zito, Tom Krauss, Utkarsh Upadhyay, Yaroslav O. Halchenko, and Yoshiki Vázquez-Baeza. SciPy 1.0: fundamental algorithms for scientific computing in Python. *Nature Methods*, 17(3):261–272, 2020.

[53] Claude Mercier. A necessary condition for hydromagnetic stability of plasma with axial symmetry. *Nuclear Fusion*, 1(1):47–53, 1960.

[54] C. C. Hegna and J. D. Callen. Stability of bootstrap current-driven magnetic islands in stellarators. *Physics of Plasmas*, 1(9):3135–3137, 1994.

[55] Matt Landreman and Wrück Sengupta. Direct construction of optimized stellarator shapes. Part 1. Theory in cylindrical coordinates. *Journal of Plasma Physics*, 84(6):905840616, 2018.

[56] John R. Cary and Svetlana G. Shasharina. Omnigenity and quasihelicity in helical plasma confinement systems. *Physics of Plasmas*, 4(9):3323–3333, 1997.

[57] J. L. Velasco, I. Calvo, F. I. Parra, and J. M. García-Regaña. KNOSOS: A fast orbit-averaging neoclassical code for stellarator geometry. *Journal of Computational Physics*, 418:109512, 2020.

[58] J. L. Velasco, I. Calvo, F. I. Parra, V. d’Herbemont, H. M. Smith, D. Carralero,

T. Estrada, and the W7-X Team. Fast simulations for large aspect ratio stellarators with the neoclassical code KNOSOS. *Nuclear Fusion*, 61(11):116013, 2021.

[59] Matt Landreman, Bharat Medasani, Florian Wechsung, Andrew Giuliani, Rogerio Jorge, and Caoxiang Zhu. SIMSOPT: A flexible framework for stellarator optimization. *Journal of Open Source Software*, 6(65):3525, 2021.

[60] Keiji Fujita, S. Satake, M. Nunami, J. M. García-Regaña, J. L. Velasco, and I. Calvo. Study on impurity hole plasmas by global neoclassical simulation. *Nuclear Fusion*, 61(8):086025, 2021.

[61] J. L. Velasco, I. Calvo, E. Sánchez, and F. I. Parra. Robust stellarator optimization via flat mirror magnetic fields. *Nuclear Fusion*, 63(12):126038, 2023.

[62] Iván Calvo, Felix I. Parra, José Luis Velasco, and J. Arturo Alonso. The effect of tangential drifts on neoclassical transport in stellarators close to omnigeneity. *Plasma Physics and Controlled Fusion*, 59(5):055014, 2017.

[63] J. H. E. Proll, G. G. Plunk, B. J. Faber, T. Görler, P. Helander, I. J. McKinney, M. J. Pueschel, H. M. Smith, and P. Xanthopoulos. Turbulence mitigation in maximum-J stellarators with electron-density gradient. *Journal of Plasma Physics*, 88(1):905880112, 2022.

[64] E. Lascas Neto, R. Jorge, C. D. Beidler, and J. Lion. Electron root optimisation for stellarator reactor designs, May 2024. arXiv:2405.12058.

[65] A. Bañón Navarro, A. Di Siena, J. L. Velasco, F. Wilms, G. Merlo, T. Windisch, L. L. LoDestro, J. B. Parker, and F. Jenko. First-principles based plasma profile predictions for optimized stellarators. *Nuclear Fusion*, 63(5):054003, 2022.